Check for updates

Earth's Future

RESEARCH ARTICLE
10.1029/2025EF007645

Hindcast Body Temperature Reveals Sites of Amplified Thermal Risk in Global Coastlines

Lin-Xuan Ma[1], Aubrey Foulk[2], Gianluca Sarà[1,3,4], Xian-Yao Chen[5], Brian Helmuth[2,6], and Yun-Wei Dong[1,7]

[1]Ministry Key Laboratory of Mariculture, Fisheries College, Ocean University of China, Qingdao, China, [2]Department of Marine and Environmental Sciences, Northeastern University Marine Science Center, Nahant, MA, USA, [3]National Biodiversity Future Centre (NBFC), Palermo, Italy, [4]Department of Earth and Marine Sciences (DiSTeM), University of Palermo, Palermo, Italy, [5]Physical Oceanography Laboratory, CIMST, Ocean University of China, Qingdao, China, [6]School of Public Policy and Urban Affairs, Northeastern University, Boston, MA, USA, [7]Shandong Key Laboratory of Green Mariculture and Smart Fishery, Fisheries College, Ocean University of China, Qingdao, China

Abstract Identifying regions where organisms are most (and least) vulnerable to climate change remains a key focus in ecological research. However, accurately capturing the thermal stress experienced by many, if not most, organisms is challenging because body temperature, which determines physiological performance, is driven by multiple environmental factors. We hindcasted hourly body temperatures of intertidal mussels globally using a modified heat budget model and assessed thermal risks (extreme temperatures and heatwaves) and hotspots based on body temperature. Results indicated that 98.34% of global coastal mussel populations faced at least one thermal risk factor, and 45.14% are subjected to the compounding effects of four or more thermal risk factors. Regions such as the Mediterranean coast and the northeastern coast of South America face a high and stacking thermal risk. Most thermal risk metrics exhibited a patchy, mosaic distribution. Semi-enclosed topography and western boundary currents are thermal risk amplifiers, making organisms in these regions more vulnerable than those in other regions of the same latitude. Our research demonstrates the utility of hindcast body temperature in integrating multiple thermal metrics to assess global thermal risks.

Plain Language Summary Climate change is making environments warmer, but how this affects organisms depends on the body temperatures they experience rather than just the air or water temperatures. For species such as intertidal mussels, body temperature can change rapidly with sunlight, wind, and tides. Here, we used a model to estimate hourly body temperatures of coastal mussels worldwide and developed a multi-metric thermal risk assessment framework based on body temperature. Our results showed that almost all mussel populations worldwide (about 98%) have faced at least one kind of thermal risk. These risks are not evenly spread, but have a patchy pattern along the world's coastlines. We found that enclosed coastlines, such as bays, and regions influenced by western boundary currents tend to be more dangerous for mussels. Finally, our study provided a clearer picture of how climate change affects coastal ecosystems. This approach helps scientists better understand where and when coastal organisms are most vulnerable to thermal stress.

Key Points:

- Thermal risk displays a patchy, mosaic distribution rather than following simple latitudinal gradients
- Regions such as the Mediterranean coast and the northeastern coast of South America face a high and stacking thermal risk
- Semi-enclosed coastlines and western boundary currents act as amplifiers for local thermal vulnerability

Supporting Information:

Supporting Information may be found in the online version of this article.

Correspondence to:

Y.-W. Dong,
dongyw@ouc.edu.cn

Citation:

Ma, L.-X., Foulk, A., Sarà, G., Chen, X.-Y., Helmuth, B., & Dong, Y.-W. (2026). Hindcast body temperature reveals sites of amplified thermal risk in global coastlines. *Earth's Future*, *14*, e2025EF007645. https://doi.org/10.1029/2025EF007645

Received 31 OCT 2025
Accepted 27 APR 2026

Author Contributions:

Conceptualization: Brian Helmuth, Yun-Wei Dong
Data curation: Lin-Xuan Ma, Aubrey Foulk
Formal analysis: Lin-Xuan Ma, Aubrey Foulk
Funding acquisition: Yun-Wei Dong
Methodology: Lin-Xuan Ma, Brian Helmuth
Project administration: Yun-Wei Dong
Resources: Yun-Wei Dong
Software: Lin-Xuan Ma
Supervision: Yun-Wei Dong
Validation: Lin-Xuan Ma, Aubrey Foulk
Visualization: Lin-Xuan Ma
Writing – original draft: Lin-Xuan Ma, Aubrey Foulk

© 2026. The Author(s).
This is an open access article under the terms of the Creative Commons Attribution License, which permits use, distribution and reproduction in any medium, provided the original work is properly cited.

1. Introduction

Accurately assessing current and future thermal risk levels remains a central concern in climate change ecology (Pigot et al., 2023; Pottier et al., 2025; Sully et al., 2022; Trew & Maclean, 2021). While global temperatures show an increasing upward trend, heterogeneity in space and time can be high, with some areas changing much more rapidly than others (Seabra et al., 2019). Spatial variation in temperature, for example, helps inform conservation planning by identifying where conditions are changing either faster or slower than surrounding areas (Helmuth et al., 2006). Similarly, global warming trends are punctuated by interannual variation as well as shorter-term extreme events (heat waves and cold snaps) that can have severe ecological impacts (Raymond et al., 2022). Most estimates of these spatial and temporal patterns are based on air, land surface, or sea surface temperature because these data are readily available over large areas and have now been collected for long periods of time. However, it is also widely understood that body temperature (and not environmental temperature) is what drives the physiological performance and survival of organisms, and for many organisms, these two metrics can be substantially different from one another (Sinclair et al., 2016). The substantial discrepancy between body temperature and the surrounding environmental temperature thus poses a major challenge to large-scale thermal risk

Writing – review & editing: Gianluca Sarà, Xian-Yao Chen, Brian Helmuth, Yun-Wei Dong

assessment and warning (Denny & Harley, 2006; Foulk et al., 2024; Ma et al., 2024). Foulk et al. (2024), for example, have argued for the use of "organismal climatology" that bases trends and spatio-temporal patterns of thermal stress on measurements and models of body temperature.

Body temperature regimes in certain habitats, such as the intertidal zone, deviate more substantially from environmental temperatures due to various factors influencing the body temperatures of organisms, particularly sessile species like mussels and oysters (Harley, 2008). The intertidal zone is a transitional zone between land and sea, where organisms in these habitats encounter wide variations in environmental conditions driven by both terrestrial and marine habitats. The cyclic transitions between aerial exposure are driven by tidal rhythms, which vary from location to location and have been shown to create complex latitudinal patterns in thermal exposure in some locations, like the west coast of North America (Helmuth et al., 2002). At much more local scales, during low tides, the body temperatures of intertidal organisms are strongly driven by exposure to solar radiation and the effects of wind velocity on convection, which are significantly affected by substrate topography (Seabra et al., 2011). While these interacting factors make predictions of thermal stress challenging, they also make the intertidal zone an excellent model system for examining the complexities of how communities respond to climate change over a range of temporal and spatial scales (Harley, 2008; Hawkins et al., 2008).

Several decades of research by a number of authors have focused on measuring and modeling the body temperatures of intertidal organisms, many with the goal of directly linking those temperatures to estimates of physiological performance (Li et al., 2021). Biomimetic sensors that mimic the thermal characteristics of key intertidal species, such as mussels (Fitzhenry et al., 2004), seastars (Szathmary et al., 2009), and limpets (Lima & Wethey, 2009) have provided long-term measurements of body temperature and frequently have shown that the patterns revealed by these data sets are radically different from those made using environmental data (air or water temperature) alone (Foulk et al., 2024; Kroeker et al., 2016; Seabra et al., 2011). Due to the expenses and difficulties associated with maintaining networks of biomimetic sensors, these data sets are usually limited to a few locations (except for the global Robomussel project and the Coupled Temperature and Biodiversity Observation Network; Helmuth et al., 2016; Seabra, 2024). To this end, direct measurements have frequently been used to develop and validate Heat Budget Models (HBMs) which can then be applied over larger spatial scales using readily available environmental data, primarily air and water temperature, solar radiation, and wind velocity (Denny & Harley, 2006; Dong et al., 2017; Helmuth, 1999; Wethey et al., 2011). Typically, HBMs fall into two categories. Individual-based models have been used to explore the fine-scale influence of an organism's physical characteristics on heat flux, and have, for example, been used to explore the influence of size, shell shape, surface color and shelter-seeking behavior (Fraser, 2023; Helmuth, 1998; Miller & Denny, 2011). Approaches that are based on land surface models (Wethey et al., 2011), in contrast, often ignore fine-scale features of substrate topography and instead treat entire sections of beds as layers, which facilitates their application over entire coastlines. With the rapid development of high-resolution gridded climate data sets, it has become feasible to extend body temperature simulations to large spatial and temporal scales (Ma et al., 2024; Wethey et al., 2011). In the present study, we modeled body temperatures of key intertidal species on a global scale. We then used these data to calculate multiple metrics, including extreme temperatures, average temperatures, hotspots, and heatwaves based on body temperature (Table S1 in Supporting Information S1). These metrics are known to affect physiological performance and survival.

Specifically, we extended the existing model developed by Wethey et al. (2011), based on the NOAH land surface model (LSM) to predict intertidal rock surface temperatures (Ek et al., 2003; Wethey et al., 2011). The outputs from this model are then used as inputs to an individual-based model of mussel temperatures (Dong et al., 2017; Helmuth, 1998; Ma et al., 2024). As sessile foundation species on rocky shores, mussels face significant thermal challenges, with extreme body temperatures in numerous populations approaching or even surpassing their thermal tolerance limits (Li et al., 2021; White et al., 2023). Their extensive dispersal ability and high reproductive potential allow mussel populations to thrive along coastlines around most of the globe (Figure S1 and Table S2 in Supporting Information S1). Mussels not only form habitat structures but also serve as essential thermal refuges for other organisms (Jurgens & Gaylord, 2018). Here, we developed the HBM for a generic mussel species with a shell length of 3 cm. Our HBM allowed us to hindcast the mussels' hourly body temperatures and was validated using measured data from mussel-shaped biomimetic sensors (Robomussels) at 24 intertidal sites along the West Coast of the United States from 2000 to 2014. Using this information, we generated a global hourly body temperature database of intertidal mussels spanning 1980 to 2023, with a spatial resolution of 0.312° × 0.312°, providing an unprecedented data set for large-scale thermal risk analysis. On this basis, we

23284277, 2026, 5, Downloaded from https://agupubs.onlinelibrary.wiley.com/doi/10.1029/2025EF007645 by University Degli Studi Di Pale, Wiley Online Library on [09/07/2026]. See the Terms and Conditions (https://onlinelibrary.wiley.com/terms-and-conditions) on Wiley Online Library for rules of use; OA articles are governed by the applicable Creative Commons License

23284277, 2026, 5, Downloaded from https://agupubs.onlinelibrary.wiley.com/doi/10.1029/2025EF007645 by University Degli Studi Di Pale, Wiley Online Library on [09/07/2026]. See the Terms and Conditions (https://onlinelibrary.wiley.com/terms-and-conditions) on Wiley Online Library for rules of use; OA articles are governed by the applicable Creative Commons License

calculated essential thermal metrics all based on predicted body temperature, including annual extreme high temperature (T_{99}: 99th percentile of hourly body temperature per year), hotspot frequency based on T_{99}, and annual biological heatwave days and mean intensity, including their values and long-term trends, to allow a global-scale intertidal thermal risk assessment (Table S1 in Supporting Information S1). To further unravel the mechanisms driving body temperature fluctuations during aerial exposure, we employed piecewise structural equation modeling (pSEM) to quantify the influence of hourly environmental variables, including air temperature, solar radiation, and wind speed, on these body temperatures in representative regions. Our findings highlight the need to integrate multiple thermal metrics and environmental factors that influence body temperature to capture the multidimensional nature of thermal stress. This comprehensive approach is necessary for a thorough understanding of the relationships between global thermal exposure and stress along the coastlines under ongoing global climate change.

2. Materials and Methods

2.1. Data Access

In the present study, we utilized hourly environmental data (including air temperature, solar radiation, wind speed, and cloud cover) from 1980 to 2023, which were downloaded from the National Centers for Environmental Prediction Climate Forecast System Reanalysis (CFSR) (Saha et al., 2010, 2011). The data were spatially interpolated using the inverse distance weighting (IDW) method based on Euclidean distance and standardized to 0.312° × 0.312° grid. Hourly sea surface temperature (SST) and significant height of combined wind waves and swell were downloaded from the ERA5 data set (0.25° × 0.25° resolution) (Hersbach et al., 2023), and were resampled to 0.312° × 0.312° using the IDW method. Moreover, we hindcasted hourly tidal height (H_t, units of m) using an empirical ocean tide model from multi-mission satellite altimetry (EOT20) by Tide Model Driver (TMD) 3.0 (MATLAB 2022a) (Greene et al., 2024; Hart-Davis et al., 2021). This regression parameter (P_w, units of m) of the significant wave height (H_w) converted to average wave run-up (AWR) revealed variability in physical shore properties (Gilman et al., 2006). We uniformly used a P_w of 0.25, reflecting a common sloping shore (Gilman et al., 2006; Helmuth et al., 2011). Tidal and wave heights were combined to calculate the seawater impact heights (H, units of m): $H = H_t + P_w H_w$.

Based on the hourly tidal height data, we utilized the MATLAB Signal Processing Toolbox to extract the Mean High Water of Spring Tides (MHWS), Mean High Water of Neap Tides (MHWN), Mean Low Water of Neap Tides (MLWN), and Mean Low Water of Spring Tides (MLWS) for each site. Then, we calculated the sum of the average between heights between adjacent tidal stages and the average local AWR to define the high, middle, and low intertidal heights, respectively (T. Zhang et al., 2021). Intertidal mussels predominantly inhabit the mid-intertidal zone, so we set the habitat height of intertidal mussels as the mid-intertidal height.

To establish a standardized global baseline for thermal risk, mussel body temperature was modeled based on morphological characteristics of *Mytilus galloprovincialis*. We selected this species as a representative model species because it is one of the most widely distributed intertidal mussels (Figure S1 in Supporting Information S1), and it has a standard mussel morphology with a black shell color and medium body size, which resembles other common species (e.g., *M. edulis* and *M. trossulus*). For the model parameterization, the solar absorptivity of mussel shell is 0.75 (Helmuth, 1998). The average shell length of the mussel is 30 mm, the total shell surface area of the shell is 1348.98 mm^2, the average shell projection area of direct sunlight is 269.66 mm^2 and the ground contact area is 0.05 times the total shell surface area.

2.2. Modeling for Simulating Mussel Body Temperature

2.2.1. Calculation of Body Temperatures of Intertidal Mussels

We implemented a simulation of body temperature in intertidal mussels using the HBM. To accurately reflect the rocky surface temperature of the intertidal zone, we utilized a NOAH LSM to estimate the surface temperature of intertidal rocks globally (Ek et al., 2003; Wethey et al., 2011). The LSM is a one-dimensional model based on heat budget principles and is employed by the US National Weather Service to simulate terrestrial environments. In the present study, we followed Wethey et al.'s (2011) treatment of tidal effects in the intertidal zone. We set the material of the global intertidal rocks as the most widely distributed granite. The rock depth was modeled as a non-uniform structure with 20 layers, the distribution of which included the first 10 layers, each 1 cm thick,

followed by three layers with thicknesses of 3, 5, and 15 cm, and finally 7 layers of 20 cm thickness. We simplified the LSM by omitting the evaporation and precipitation to reduce the computational effort (Denny & Dowd, 2012). To ensure convergence of the model results, we resampled the time step from 1-hr to 6-min intervals during the iterations.

We input mussel morphology, habitat height, and climatic and hydrologic variables into the HBM to predict the global body temperature of intertidal mussels (Helmuth, 1998, 1999; Helmuth et al., 2011; Ma et al., 2024). Since the mussel's tightly closed shells reduce water loss from many species, we excluded evaporative heat loss from the model. Additionally, we omitted metabolic heat generation, as their metabolic heat production and ability to retain this heat are minimal. In our analysis, we hindcasted the global body temperature from 1980 to 2023 using medium-sized (3 cm) mussels. Wind speeds are converted to near-substratum conditions using boundary layer theory (Helmuth, 1999). Previous studies indicate that medium-sized mussels reach thermal equilibrium within approximately 20–30 min, thus justifying the use of a steady-state HBM with 1 hourly time step (Helmuth et al., 2011). All model parameters are shown in Table S3 in Supporting Information S1.

2.2.2. Model Verification

To validate the HBM, we utilized the most extensive, long-term, and rigorously standardized mussel temperature data set currently (Helmuth et al., 2016). Specifically, we tested model outputs against field temperatures recorded by a series of mussel-shaped sensors (Robomussels) at 24 rocky shoreline sites along the west coast of the U.S. between 2000 and 2015. These 8 cm loggers were positioned horizontally (facing upward) in unshaded sections of the intertidal zones at a tidal elevation of MLLW +1.5 m. We processed the raw 10-min interval temperature data into hourly averages and then derived the daily maximum, mean, and minimum temperatures based on 24-hr values, which were compared to model-simulated temperatures at hourly intervals. We defined the effective shore level (ESL) as the tidal height where sudden temperature changes exceeded 4°C and estimated the correlation coefficients between the difference between the absolute shore level offset from ESL and localized significant wave heights (P_w) using SiteParser software (Gilman et al., 2006). We hindcasted hourly body temperatures from 2000 to 2015 for all model validation sites and derived the daily maximum, average, and minimum temperatures based on the model, which was compared to the results of measurements obtained using Robomussels.

The HBM was found to simulate the mussels' body temperatures accurately (Table S4 and Figure S2 in Supporting Information S1). The average error for daily maximum body temperature was −0.17 ± 4.58°C, with an RMSE of 4.58°C; the average error for daily average body temperature was −0.10 ± 1.57°C, with an RMSE of 1.58°C; and the average error for daily minimum body temperature was −0.03 ± 2.35°C, with an RMSE of 2.35°C. Because our HBM is a mechanistic first-principles biophysical model, this validation confirms its strong global transferability.

2.3. Analysis of Thermal Metrics

2.3.1. Extreme Temperature Hotspots and Biological Heatwaves

The annual T_{99} (99th percentile of hourly body temperature per year) is used to represent the acute thermal stress experienced by intertidal mussels. Identifying extreme temperature hotspots in the intertidal zone (i.e., areas where local extreme temperatures are significantly higher than surrounding regions) offers valuable insights for assessing thermal risks to mussels. We define a 50 km radius as a unit (the estimated poleward shift distance per decade of intertidal biota) and calculate the average T_{99} within this radius. If the T_{99} in a given area exceeds the 90th percentile threshold of T_{99} within a 500 km radius, that coastal pixel is designated as a T_{99} hotspot.

We calculated biological heatwave events globally for intertidal mussels. Using a methodology like that used to characterize marine heatwaves, we defined events where the daily average body temperature exceeds the 90th percentile of local seasonal variation and persists for at least 5 consecutive days as intertidal biological heatwaves. The baseline climate period was defined from 1 January 1981, to 31 December 2010, covering 30 years. To mitigate the influence of spring and neap tides (with a period of 14.8 days), we extended the sliding window width for comparing heatwave temperature thresholds to 15 days. We then calculated the annual heatwave days and heatwave intensity to represent the spatiotemporal patterns of thermal stress of heatwaves.

23284277, 2026, 5, Downloaded from https://agupubs.onlinelibrary.wiley.com/doi/10.1029/2025EF007645 by University Degli Studi Di Pale, Wiley Online Library on [09/07/2026]. See the Terms and Conditions (https://onlinelibrary.wiley.com/terms-and-conditions) on Wiley Online Library for rules of use; OA articles are governed by the applicable Creative Commons License

23284277, 2026, 5, Downloaded from https://agupubs.onlinelibrary.wiley.com/doi/10.1029/2025EF007645 by University Degli Studi Di Pale, Wiley Online Library on [09/07/2026]. See the Terms and Conditions (https://onlinelibrary.wiley.com/terms-and-conditions) on Wiley Online Library for rules of use; OA articles are governed by the applicable Creative Commons License

2.3.2. Trend Calculations

For spatial trend mapping, we used the Mann-Kendall trend test to assess the significance of trends in the thermal metrics and applied a generalized linear model (GLM) to calculate the linear trend of climatic variables at each site. To account for temporal autocorrelation and improve the accuracy of long-term trend estimation at the global scale, we applied ARIMA models to the globally averaged annual time series of the thermal metrics (i.e., T_{99}, T_{mean}, heatwave days, and heatwave mean intensity; Shumway et al., Springer International Publishing, 2017). Model selection followed standard procedures: the Augmented Dickey-Fuller (ADF) test checked stationarity; the Autocorrelation Function (ACF) and Partial Autocorrelation Function (PACF) guided model selection; the Akaike Information Criterion (AIC) determined the optimal model order (p, d, q); the residual diagnostics assessed model adequacy. The results showed that the optimal model orders of all temperature series are d = 1, so we extracted the drift term to represent the long-term trend under climate change. Detailed ARIMA diagnostic results, including Ljung-Box tests and residual plots for the four global metrics, are provided in the Supplementary Information (Table S5 and Figure S3 in Supporting Information S1).

2.3.3. Overlaying Thermal Risks for Intertidal Mussels

We set thermal risk thresholds for multiple thermal metrics, including extreme heat, hotspot frequency, annual heatwave days, and heatwave mean intensity, to develop a scoring system that translates thermal stress into absolute risk categories (Bagne et al., 2011; Boyce et al., 2022) (Table S1 in Supporting Information S1). This approach was informed by the extinction risk definitions of the IUCN Red List of Species and the Reasons for Concern framework adopted by the International Plant Protection Convention (IPCC, 2021; IUCN, 2024). Each metric was assigned a three-level score (0–1–2) corresponding to low, moderate, and high risk. Thresholds were set as follows: T_{99} (<30°C = 0; 30–45°C = 1; >45°C = 2) (Table S6 in Supporting Information S1) (Halpin et al., 2004; Li et al., 2021; Seuront et al., 2019; Tagliarolo & McQuaid, 2015); annual heatwave days (<15 = 0; 15–30 = 1; >30 = 2) (Coelho et al., 2023; Holbrook et al., 2019; Ma et al., 2024); heatwave mean intensity (<3°C = 0; 3–4°C = 1; >4°C = 2) (Holbrook et al., 2019; Ma et al., 2024; Raymond et al., 2022); hotspot frequency (0 = 0; 0–0.5 = 1; >0.5 = 2). We then established a five-level trend scoring system (−2 to 2) for the thermal stress trends in extreme high temperatures, annual heatwave days, and heatwave mean intensity. Non-significant trends were scored 0, while significant trends were assigned −1/1 (moderate decrease/increase) or −2/2 (strong decrease/increase) based on predefined statistical thresholds (e.g., 0.05°C per year for extreme temperature, 1 day yr^{-1} for heatwave days, and 0.04°C per year for mean intensity). Using the MEOW (Marine Ecoregions of the World) biogeographic zones, we delineated 11 high-risk zones for global intertidal regions: Central Indo-Pacific, Northwest Pacific, Asia Arctic, European Atlantic, Mediterranean-Black Sea, Arabian Peninsula, East Africa, South Australia, Northwest Atlantic, Central America and Gulf of Mexico, and South America Eastern (Spalding et al., 2007).

2.3.4. Thermal Risk Attribution

To assess the direct and indirect effects of various hourly environmental indicators on the body temperature of intertidal mussels during low tide emersion, we employed a hierarchical (linear) mixed-effects model implemented through the "piecewiseSEM" R package (Lefcheck, 2016). The model evaluated the relationships between various hourly environmental variables (air temperature, solar radiation, wind speed, and cloud cover) and the body temperature in representative regions (e.g., the Mediterranean Sea and the Black Sea, the Japan Sea, the Persian Gulf, the Gulf of Mexico, the coasts affected by Kuroshio Current, and the coasts affected by Gulf Stream & Equatorial Current in Northern Hemisphere). We classified explanatory variables into endogenous variables and exogenous variables. During data processing, we checked for multicollinearity among variables using the Variance Inflation Factor (VIF), ensuring that no significant multicollinearity existed between the explanatory factors (VIF <5). We standardized all data within each site and used the "lme" function in the "nlme" package (Pinheiro et al., 2011). To account for spatial non-independence and baseline differences across different locations, we incorporated sampling sites as a random intercept in the models (i.e., random = ~1|Site). Finally, we quantified each variable's direct and indirect path coefficients, providing deeper insights into how environmental changes are associated with the thermal stress of intertidal mussels during low tide emersion.

23284277, 2026, 5, Downloaded from https://agupubs.onlinelibrary.wiley.com/doi/10.1029/2025EF007645 by University Degli Studi Di Pale, Wiley Online Library on [09/07/2026]. See the Terms and Conditions (https://onlinelibrary.wiley.com/terms-and-conditions) on Wiley Online Library for rules of use; OA articles are governed by the applicable Creative Commons License

2.4. Statistical Analysis

We averaged thermal metrics within 0.312° latitudinal intervals for the eastern and western coasts of the North American, and for the eastern and western coasts of the combined Asian and European continents (including adjacent parts of North Africa), to compare thermal stress differences between the east and west coasts of continents at mid-latitudes of the Northern Hemisphere (20–60°N). Paired *t*-tests were conducted to assess differences in thermal metrics, and the normality of the differences was evaluated using Kolmogorov-Smirnov tests.

To quantify spatial heterogeneity in mean and extreme body temperatures, we calculated Moran's I for each year at the global scale, using inverse-distance weighting based on Euclidean distances. We compared the Moran's I values of mean versus extreme body temperatures using paired *t*-tests, and assessed the normality of their differences with Kolmogorov-Smirnov tests.

We compared the trend of regional thermal metrics with global trends using one-sample Welch's *t*-tests. Furthermore, we quantified effect sizes using Cohen's d. To account for multiple comparisons across these regions, we applied a false discovery rate (FDR) correction using the Benjamini–Hochberg procedure with significance determined at an adjusted alpha level of 0.05.

To calculate the proportion of coastline area with significant trends of thermal stress, we accounted for the latitudinal variation in grid size by incorporating the cosine of latitude when estimating the actual surface area represented by each coastal pixel.

3. Results

3.1. Global Spatial Patterns of Thermal Stress in Intertidal Mussels

We set the annual T_{99} (i.e., the 99th percentile of hourly body temperatures per year) for characterizing the annual extreme heat experienced by intertidal mussels. From 1980 to 2023, the global annual T_{99} values have ranged from 3.59°C to 53.32°C, with a median of 24.22°C (Figure 1a). Compared to mean body temperatures, the spatial distribution of annual T_{99} showed significant spatial heterogeneity, forming a mosaic pattern (Figures 1a and 1c), but with an overall decline toward higher latitudes, as expected. In the Northern Hemisphere, the latitudinal decrease averaged 0.52°C per degree ($R^2 = 0.93$, $p < 0.01$), while in the Southern Hemisphere, it is 0.54°C per degree ($R^2 = 0.97$, $p < 0.01$) (Figure 1b). On a global scale, the coastal regions of the Central Indo-Pacific, Arabian Peninsula, and Central America experienced the highest body temperatures (Table S7 in Supporting Information S1).

We identified coastal extreme temperature hotspots by comparing the average T_{99} within a 50 km radius against the 90th percentile of T_{99} values from all coastal sites within a surrounding 500 km region. We found that hotspots are distributed ubiquitously, and permanent hotspots are concentrated in semi-closed seas, including major bays (e.g., Gulf of California), inland seas (e.g., Mediterranean Sea), narrow straits (e.g., Strait of Malacca), estuaries (e.g., Río de la Plata), and interisland straits in archipelagos (e.g., the Philippine Archipelago; Figure S4 in Supporting Information S1).

The spatial patterns of heatwaves based on average daily body temperatures differed notably from the extreme heat (Figure 1e). Specifically, annual heatwave days were significantly higher in the Northern Hemisphere (17.81 ± 8.43°C) than in the Southern Hemisphere (10.19 ± 7.94°C) ($p < 0.01$, Cohen's d = 0.92). The mean intensity of heatwaves followed a distinct latitudinal pattern, with the highest intensities (>5°C) observed at the poles (Figures 1g and 1h). In the Northern Hemisphere, the mean intensity increased by 0.04°C per degree of latitude ($R^2 = 0.88$, $p < 0.01$), but decreased slightly in the Southern Hemisphere with 0.002°C per degree of latitude ($R^2 = 0.02$, $p < 0.01$). Notably, heatwave intensity was significantly stronger on the eastern than on the western coasts of continents in the mid-latitudes of the Northern Hemisphere. Paired *t*-tests confirmed that heatwave intensities on the east coast of North America ($t(126) = 19.55$, $p < 0.01$) and Eurasian continent ($t(127) = 18.11$, $p < 0.01$) were significantly higher than on the west coast.

3.2. Multidecadal Changes in Thermal Stress of Intertidal Mussels

A rapid global increase in the body temperatures of intertidal mussels occurred from 1980 to 2023, with warming rates of 0.25 ± 0.07°C per decade for mean temperatures and 0.20 ± 0.12°C per decade for extreme high temperatures (Figures 2a, 2b, 2e, and 2f). Specifically, 84.02% of the coastlines exhibited an increasing trend in

10.1029/2025EF007645

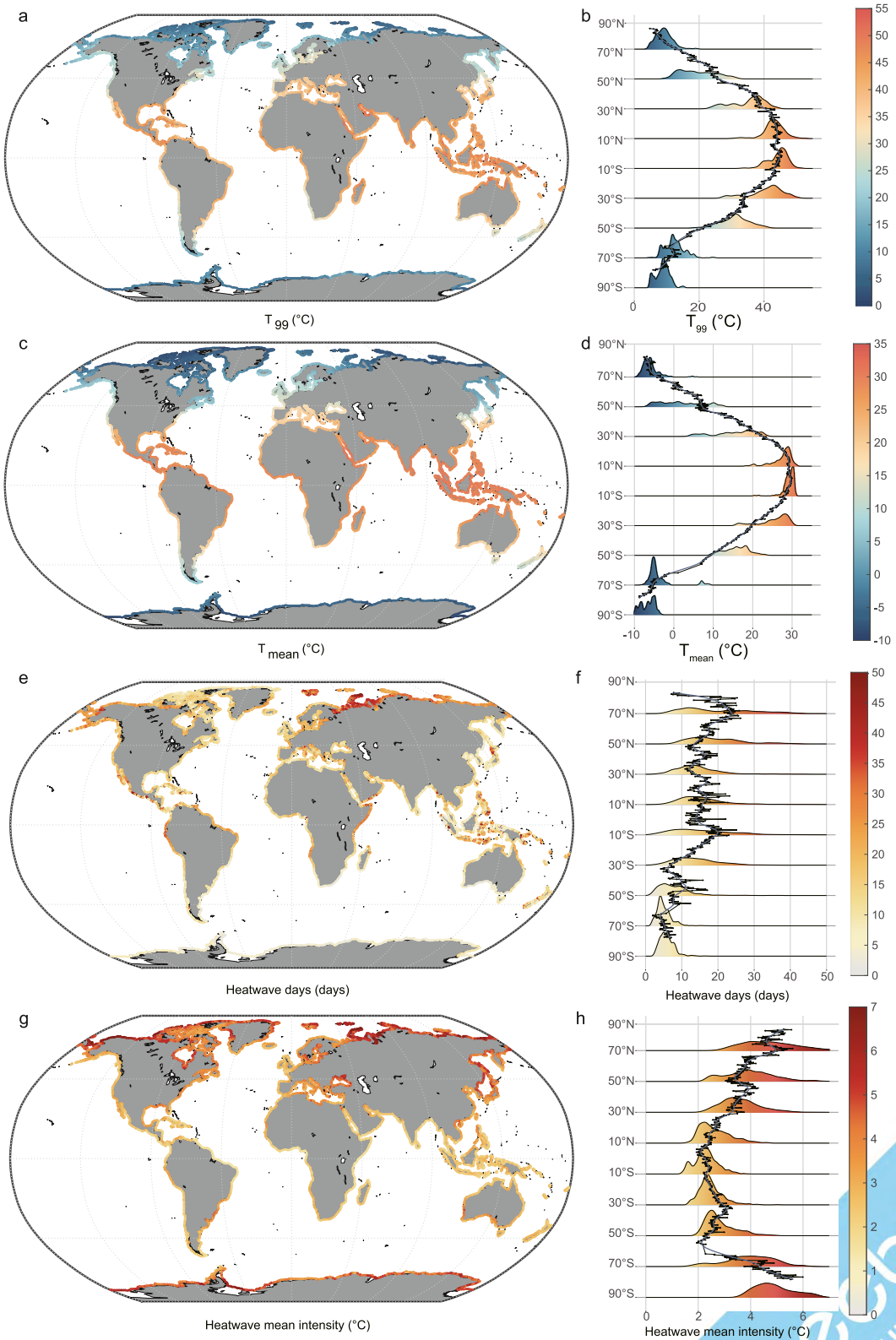


Figure 1.

23284277, 2026, 5, Downloaded from https://agupubs.onlinelibrary.wiley.com/doi/10.1029/2025EF007645 by University Degli Studi Di Pale, Wiley Online Library on [09/07/2026]. See the Terms and Conditions (https://onlinelibrary.wiley.com/terms-and-conditions) on Wiley Online Library for rules of use; OA articles are governed by the applicable Creative Commons License

23284277, 2026, 5, Downloaded from https://agupubs.onlinelibrary.wiley.com/doi/10.1029/2025EF007645 by University Degli Studi Di Pale, Wiley Online Library on [09/07/2026]. See the Terms and Conditions (https://onlinelibrary.wiley.com/terms-and-conditions) on Wiley Online Library for rules of use; OA articles are governed by the applicable Creative Commons License

mean temperatures, 10.99% showed no significant change, and 4.99% showed a decreasing trend. Meanwhile, 49.63% of the coastlines showed an increasing trend in extreme temperatures, 39.03% showed no significant change, and 11.33% showed a decreasing trend.

Compared to mean body temperatures, changes in extreme body temperatures exhibited higher spatial heterogeneity (paired *t*-tests, $t(43) = -7.37$, $p < 0.01$; Figures 2a and 2b). The coasts of the Mediterranean Sea and the Black Sea, the coast of the White Sea, the Barents Sea and Kara Sea and the coast of the Japan Sea exhibited notably high warming rates, with average rates of 0.42 ± 0.57°C ($p < 0.01$, Cohen's $d = 0.42$), 0.46 ± 0.41°C ($p < 0.01$, Cohen's $d = 0.54$), and 0.43 ± 0.41°C ($p < 0.01$, Cohen's $d = 0.46$) per decade, respectively.

The annual heatwave days experienced by intertidal mussels have significantly increased, at 0.86 ± 0.27 days per year (Figures 2c and 2g). Specifically, 80.24% of the coastlines experienced a significant increase, 18.17% remained stable, and only 1.59% decreased in heatwave days. The western coast of South America is a key region exhibiting a decrease in heatwave days. In contrast, the coast of the White Sea, the Barents Sea and the Kara Sea showed the strongest rise (2.47 ± 0.58 days per year, $p < 0.01$, Cohen's $d = 2.03$) (Table S8 in Supporting Information S1).

Globally, the annual mean intensity of heatwaves showed no uniform trend(-0.09 ± 0.01°C per decade) (Figures 2d and 2h). Polar regions tend to experience a decrease in intensity, while equatorial and mid-latitude regions show an increasing trend in intensity. Coastal regions such as the Caribbean coast of Panama and Colombia (0.17 ± 0.15 days per decade, $p < 0.01$, Cohen's $d = 1.02$) showed a rapid increase in heatwave intensity (Table S8 in Supporting Information S1).

3.3. Global Thermal Risk Assessment

Thermal risk scores are derived from thermal risk factors, including the values and trends of extreme body temperature and heatwaves, to identify which regions are more thermally vulnerable (see Table S1 and Figure S5 in Supporting Information S1). The risk scores for intertidal mussels range from a maximum of 11 to a minimum of −3 (Figure 3a). Among the assessed regions, 42.13% of global coastlines exceeded a score of 5, while only 2.01% fell below zero. As indicated by the thermal risk scores, high-risk regions exhibited a patchy distribution pattern across latitudes, and 98.34% of the area was affected by at least one thermal risk factor, whereas 45.14% was subject to the overlapping of four or more thermal risk factors (Figure 3). Higher-risk coastal regions were concentrated in semi-enclosed seas, coasts affected by Northern Hemisphere western boundary currents, and the Arctic coast. The analysis revealed that these globally representative regions consistently exhibit significantly higher thermal risk scores compared to the global mean (All $p < 0.001$) (Figure 3b).

Using the MEOW biogeographic zones and the thermal risk scores, we identified 11 critical high-risk coastal regions: Central Indo-Pacific, Northwest Pacific, Asia Arctic, European Atlantic, Mediterranean-Black Sea, Arabian Peninsula, East Africa, Gulf of Guinea, Northwest Atlantic, Central America and Gulf of Mexico, and Eastern South America (Figure 4 and Table S9 in Supporting Information S1). The causes of thermal stress in these high-risk regions vary substantially. For instance, the Central Indo-Pacific and Arabian Peninsula were the highest-scoring regions for T_{99}, with Halmahera (ECOID: 129) in the Central Indo-Pacific and the Arabian Gulf (ECOID: 90) in the Arabian Peninsula being the most severely affected regions, with 96.30% and 94.12% of the regions falling under high-risk conditions for T_{99} (>45°C), respectively. Annual heatwave days posed the greatest risk to Arctic Asia, and annual heatwave mean intensity poses the greatest risk to Arctic Asia, the Mediterranean-Black Sea regions, and the Northwest Pacific. Hotspot distribution varied considerably within these regions. For example, the Central Kuroshio Current (ECOID: 51) in the Northwest Pacific had 16.67% of its area experiencing frequent hotspots (hotspot frequency >50%), while the Oyashio Current (ECOID: 47) did not have regions experiencing hotspots. In all high-risk regions, the trend for global thermal metrics generally indicated an

Figure 1. Global spatial patterns of thermal metrics for mussels. (a, c, e, g) Global maps of four thermal metrics: extreme high temperature (T_{99}) (a), mean body temperature (c), heatwave days (e), and heatwave mean intensity (g). (b, d, f, h) Latitudinal patterns of four thermal metrics: extreme high temperature (T_{99}) (b), mean body temperature (d), heatwave days (f), and heatwave mean intensity (h). Kernel density curves are plotted at 20-degree latitude intervals, with bandwidth determined using Silverman's rule of thumb. Thermal metrics are averaged at a 0.312° latitude interval and are represented by black line plots. These data are further smoothed using locally weighted scatterplot smoothing (LOESS) filtering (0.1 fraction), shown as a dark blue curve.

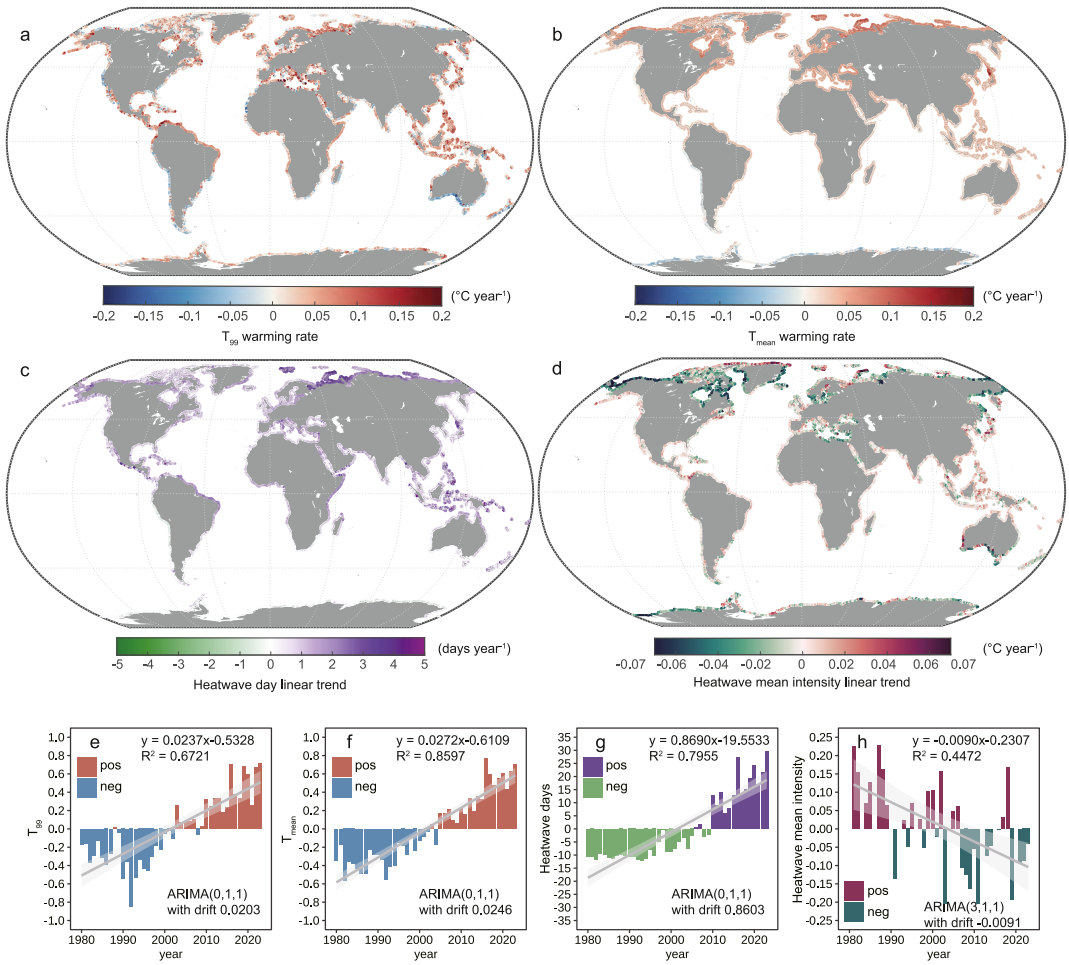


Figure 2. Global temporal dynamics of thermal metrics for mussels. (a–d) Global maps of the linear trends of four thermal metrics under climate change: extreme high temperature (T_{99}) (a), mean body temperature (b), heatwave days (c), and heatwave mean intensity (d). The Mann-Kendall trend test was applied to assess the statistical significance of trends in each coastal pixel, with significant trends marked by a small black dot. (e–h) Anomaly values of the four thermal metrics: extreme high temperature (T_{99}) (e), mean body temperature (f), heatwave days (g), and heatwave mean intensity (h), using 1980–2023 as the baseline period. Positive and negative anomalies are distinguished by two different colors. Gray lines plotted using the generalized linear models (GLM) represent the trend for each thermal metric, with the 95% confidence interval represented by a light gray shading. The results of the ARIMA model for each thermal metric are displayed in the lower right corner of panels (e–h).

increasing pattern. In the Mediterranean and Black Sea, 96.24% of the regions face risk conditions due to an increase in the occurrence of heatwave days per year.

3.4. Driver Factor Analysis

We built pSEMs to assess the direct and indirect effects of hourly environmental variables on body temperature during aerial exposure (Figure 5 and Figure S7 in Supporting Information S1), using data from six representative regions during the aerial exposure phase between 1980 and 2023. Across all regions, the models demonstrated high variable explanatory power for hourly body temperatures ($R^2 \geq 88.93\%$). Solar radiation and air temperature were the dominant environmental factors, with mean total effects of 0.78 ± 0.11 and 0.59 ± 0.14, respectively. Notably, along the coast of the Sea of Japan, air temperature exhibited a stronger positive association (total effect = 0.81) than solar radiation (0.58). In addition, wind speed was consistently negatively associated with body temperature across all regions, with a mean total effect of -0.15 ± 0.05. Cloud cover had weak but variable relationships, with a mean total effect of -0.02 ± 0.09. It is worth noting that body temperatures in the Mediterranean Sea and the Black Sea demonstrated a stronger negative correlation with cloud cover, with a total effect of -0.18.

23284277, 2026, 5, Downloaded from https://agupubs.onlinelibrary.wiley.com/doi/10.1029/2025EF007645 by University Degli Studi Di Pale, Wiley Online Library on [09/07/2026]. See the Terms and Conditions (https://onlinelibrary.wiley.com/terms-and-conditions) on Wiley Online Library for rules of use; OA articles are governed by the applicable Creative Commons License

10.1029/2025EF007645

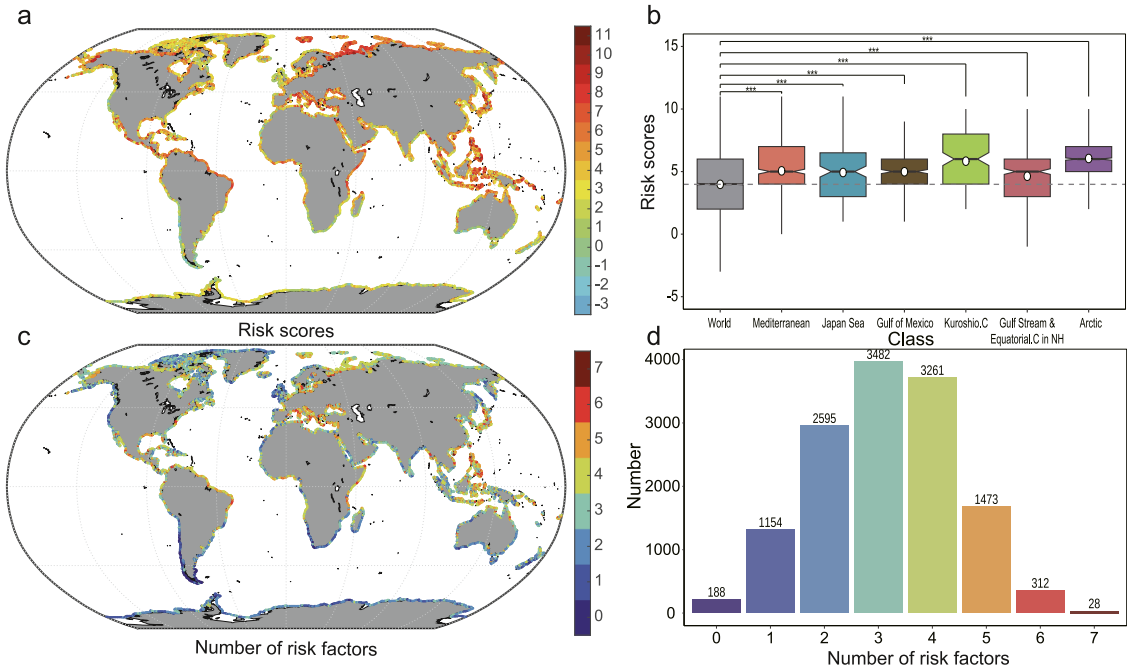


Figure 3. Global thermal risk scores. (a) Global thermal risk score map derived from the assessment of thermal stress based on extreme high temperature, hotspot frequency, heatwaves, and their change rates. Regions that are impacted by multiple thermal stresses and are more strongly impacted tend to have higher scores. (b) Box plots of risk scores globally and for representative semi-enclosed seas, western boundary currents and polar regions (see Figure S6 in Supporting Information S1). The top and bottom edges of the box indicate the 25th percentile (Q1) and the 75th percentile (Q3), and the middle horizontal line indicates the median (50th percentile). The top and bottom must indicate values that do not exceed the range of 1.5 times the interquartile range (IQR). White dots indicate mean values. The use of a gray dotted line indicates the average risk score for the global coastline. One-way ANOVA was used to compare the differences in risk scores between regions and the global average. (c) Global thermal risk factors number map, representing the count of thermal metrics contributing to the thermal risk score. The higher the value, the higher the thermal risk to which the region is exposed. (d) Histogram of the distribution of risk factor exposures, with the horizontal axis indicating the number of risk factor exposures and the vertical axis indicating the number of pixels corresponding to the number of risk factor exposures.

4. Discussion

4.1. Global Distribution Patterns of Thermal Risks

Our risk assessment identified high-risk regions, primarily located in semi-enclosed seas and coasts influenced by western boundary currents. A semi-enclosed sea is a water body, that is, surrounded by land but still connected to the open seas through one or more narrow waterways, including bays, inland seas, lagoons, narrow straits, estuaries, seas surrounded by island chains, and inter-island straits in an archipelago. Higher water temperatures in semi-enclosed seas compared to those of adjacent open oceans contribute to the formation of locally warmer climates (Feng et al., 2018). For example, in the Šćuza Lagoon in Croatia, summer daily average water temperatures were observed to be up to 5°C higher than those outside of this lagoon (Bilajac et al., 2024). This may be attributed to several factors. First, semi-enclosed seas have longer water residence times than open seas, allowing greater heat accumulation and, thus, the potential for extreme temperatures (H. Zhang et al., 2021). Second, semi-enclosed seas often develop thermal stratification, trapping heat in the upper water layers, and lack upwelling of cooler waters (Shunk et al., 2024). Third, semi-enclosed seas experience more pronounced land-based influences than open seas, leading to greater seasonal temperature variations (Stock et al., 2015). Aside from higher water temperatures, other factors also amplify the thermal risk to mussels in semi-enclosed areas. Terrain-induced wind sheltering in semi-enclosed seas with a narrow wind fetch weakens convective heat dissipation between the shell and surrounding air during extreme high temperatures (Cavaleri et al., 2024). Additionally, eddies formed within semi-enclosed seas create dynamic barriers that restrict the movement of larvae and plankton, potentially severely limiting the dispersal of mussels under climate change (Sánchez-Velasco et al., 2025), and rendering semi-enclosed seas "thermal traps."

Coastlines impacted by western boundary currents are high-risk areas in the context of global climate change. The western boundary currents are narrow, fast-warming currents found in all major ocean circulations that increase

23284277, 2026, 5, Downloaded from https://agupubs.onlinelibrary.wiley.com/doi/10.1029/2025EF007645 by University Degli Studi Di Pale, Wiley Online Library on [09/07/2026]. See the Terms and Conditions (https://onlinelibrary.wiley.com/terms-and-conditions) on Wiley Online Library for rules of use; OA articles are governed by the applicable Creative Commons License

10.1029/2025EF007645

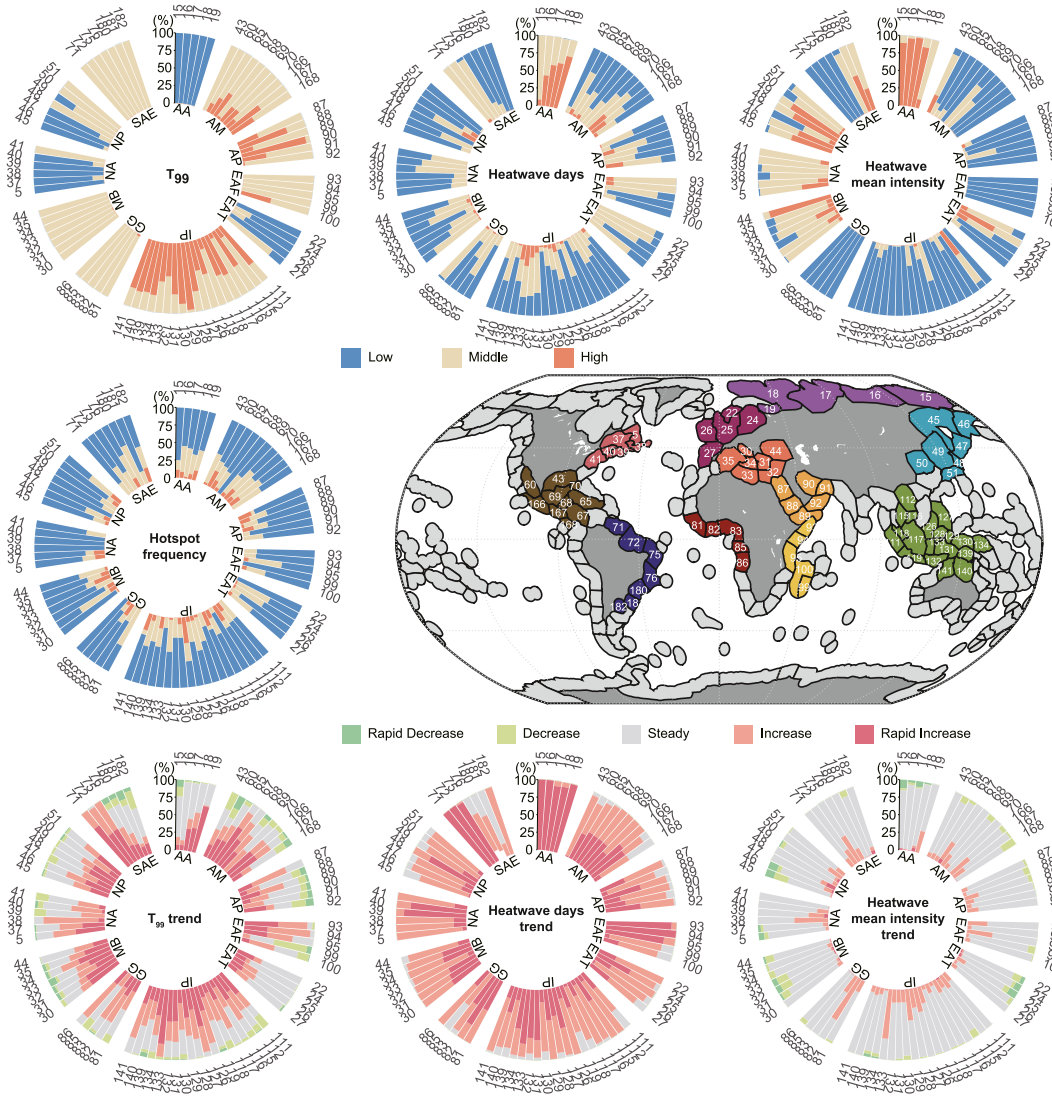


Figure 4. Overview of global high-risk regions for mussels. Based on the spatial distribution of thermal metrics and their trends, as well as the global thermal risk score map, we identified 11 high-risk regions for mussels worldwide (based on the Marine Ecoregions of the World, MEOW) and labeled them using EcoCode. These regions include the Central Indo-Pacific (IP, green), Northwest Pacific (NP, light blue), Asia Arctic (AA, purple), European Atlantic (EAT, dark magenta), Mediterranean-Black Sea (MB, orange), Arabian Peninsula (AP, golden), East Africa (EAF, light yellow), South Australia (SA, brick red), Northwest Atlantic (NA, pink), Central America and Gulf of Mexico (AM, brown), and South America Eastern (SAE, dark blue). We used Nightingale rose diagrams to illustrate the thermal risk scores of coastal pixels for each thermal metric within the biogeographic ecoregions of each high-risk region.

adjacent shelf temperatures (Larson et al., 2024; Yang et al., 2025). Major western boundary current extensions in the Northern Hemisphere, such as the Kuroshio extension in the North Pacific, have high thermal risk scores due to their unique thermal characteristics. The western boundary currents in the Southern Hemisphere, except for the Agulhas Current, which amplifies thermal risk along the coast of Madagascar, generally exhibit limited thermal risk amplification. This is particularly evident in major warm currents like the Brazil Current, which can be attributed to their relatively low thermal transport capacity (Talley, 2011). Furthermore, it has been shown that the western boundary current extensions exhibit the most pronounced warming and highly dynamic marine heatwaves (Wu et al., 2012). As climate change intensifies, temperatures and heatwaves are expected to increase in coastal regions affected by western boundary currents (Holbrook et al., 2019; Yang et al., 2025). Compared to the eastern boundary currents, which transport cold water and reinforce upwelling to create thermal refuges, the western boundary currents bring surface low-density warm water that may consolidate thermal stratification.

23284277, 2026, 5, Downloaded from https://agupubs.onlinelibrary.wiley.com/doi/10.1029/2025EF007645 by University Degli Studi Di Pale, Wiley Online Library on [09/07/2026]. See the Terms and Conditions (https://onlinelibrary.wiley.com/terms-and-conditions) on Wiley Online Library for rules of use; OA articles are governed by the applicable Creative Commons License

10.1029/2025EF007645

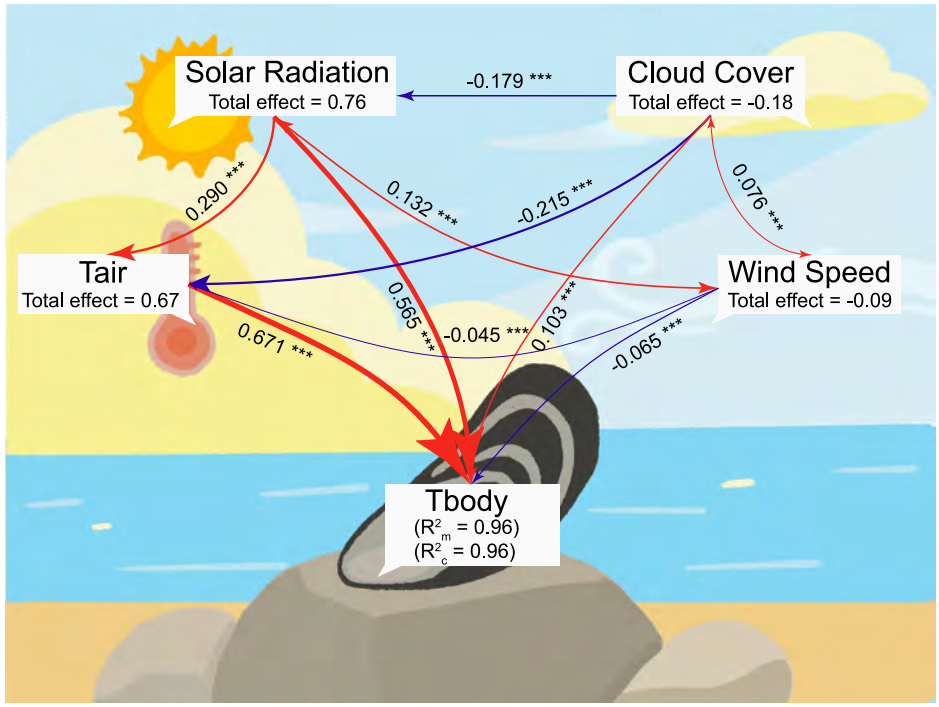


Figure 5. Attribution of hourly body temperature in mussels during low tide emersion for the Mediterranean Sea and the Black Sea. pSEM illustrated the direct and indirect effects of various environmental variables on hourly body temperature. Red solid arrows indicate significantly positive associations, blue solid arrows indicate significantly negative associations, and gray dashed arrows indicate non-significant relationships. Standardized coefficients and their *p*-value ranges are labeled alongside the solid arrows (* for $p < 0.05$; ** for $p < 0.01$; *** for $p < 0.001$). The thickness of each solid arrow is proportional to its standardized coefficient. The total effects of environmental variables on the body temperature are represented in the boxes of environmental variables. The R^2 values inside the boxes of Tbody represent the proportion of variance explained by this model.

Some studies suggest that western boundary currents facilitate the poleward dispersal of mussel larvae and buffer populations against warming. However, the enhanced strength of these currents under climate change may introduce new challenges to mussel persistence (Wilson et al., 2016).

4.2. Thermal Metrics and Risk Attribution

During the low-tide phase, intertidal organisms are subjected to a complex interplay of environmental factors, and extreme body temperatures are most likely to occur then. Our pSEM results indicated that solar radiation is a dominant predictor of body temperatures (Mislan et al., 2009). When low tide coincides with periods of intense solar radiation, body temperatures can spike rapidly, deviating substantially from air temperature. In contrast, if low tide occurs at night or under strong winds, air temperature may become the dominant thermal predictor. Along the coast of the Sea of Japan, air temperature exerts a stronger statistical association than solar radiation, likely due to the short duration and low intensity of solar radiation, and the high wind speeds in the region (Young et al., 2020). Although the overall statistical relationship between cloud cover and body temperature is relatively weak, it results from opposing mechanisms: cooling from reduced solar input during the day and warming from enhanced longwave radiation at night. Thus, even a modest cloud effect warrants attention, especially in regions with intense daytime solar input. In the Mediterranean Sea and the Black Sea, the total effect of cloud cover on body temperature remains notably negative, likely due to the region's typically low summer cloud cover under the influence of subtropical high pressure systems. In these areas, increases in cloudiness are often linked to the arrival of cold fronts (Ioannidis et al., 2018). Water temperature, while not directly affecting body temperature during aerial exposure, can indirectly modulate body temperature by shaping air conditions through thermal inertia and convective processes (Feng et al., 2018). Lastly, regional differences in tidal actions influence the

23284277, 2026, 5, Downloaded from https://agupubs.onlinelibrary.wiley.com/doi/10.1029/2025EF007645 by University Degli Studi Di Pale, Wiley Online Library on [09/07/2026]. See the Terms and Conditions (https://onlinelibrary.wiley.com/terms-and-conditions) on Wiley Online Library for rules of use; OA articles are governed by the applicable Creative Commons License

23284277, 2026, 5, Downloaded from https://agupubs.onlinelibrary.wiley.com/doi/10.1029/2025EF007645 by University Degli Studi Di Pale, Wiley Online Library on [09/07/2026]. See the Terms and Conditions (https://onlinelibrary.wiley.com/terms-and-conditions) on Wiley Online Library for rules of use; OA articles are governed by the applicable Creative Commons License

frequency and timing of aerial exposure, playing a key role in the spatial mosaic of thermal stress patterns across intertidal zones (Helmuth et al., 2002).

4.3. Conservation and Recommendations

Our global assessment of thermal risks in intertidal mussel populations provides a novel and operational framework for integrating organismal vulnerability into conservation planning and climate-resilient marine spatial strategies. By combining multiple thermal metrics - including acute maxima, frequency of hotspots, and heatwave dynamics - we identified not only regions of elevated physiological stress (thermal hotspots), but also areas of relative thermal stability and resilience that may serve as candidates for spatial conservation prioritization, ecosystem restoration or low-impact aquaculture. These data enable the development of mechanistic climate conservation rules, whereby exposure, intensity and persistence of thermal extremes are assessed against species-specific tolerance thresholds (Queirós et al., 2021). Crucially, we also provide supporting data for the identification of thermal hotspots, that is, regions where environmental conditions are projected to remain within the adaptive envelope of specific mussels. Identifying these areas offers actionable opportunities for nature-based solutions, such as the establishment of thermally tolerant lineages, mussel-based reef restoration, or the design of climate-resilient mariculture systems (Queirós et al., 2021). Embedding physiological metrics into spatial planning enhances anticipatory governance, enabling decision-makers to shift from reactive to proactive conservation in the face of climate change (Colton et al., 2022). In addition, our results call for targeted protection strategies that account for the compound effects of heatwave timing, tidal cycles, and cumulative anthropogenic pressures. In areas experiencing frequent biological heatwaves, often coinciding with seasonal temperature anomalies and midday low tides, effective management must extend beyond spatial zoning to include the regulation of harvest, trampling, coastal pollution and habitat fragmentation (Sampaio et al., 2022). Similarly, green coastal infrastructure should be designed to enhance thermal buffering, surface complexity and habitat suitability across life stages of native intertidal species, while critically reassessing the ecological impact of wave-breakers that reduce natural splash regimes and elevate thermal stress. Finally, integrating body temperature-derived metrics rather than relying solely on abiotic proxies is essential for capturing biologically meaningful thresholds in thermal risk assessment. This approach not only enhances ecological realism but also aligns with global sustainability frameworks such as the Kunming-Montreal Global Biodiversity Framework, UN SDGs 13 and 14, and emerging best practices in climate-adaptive marine spatial planning. As intertidal systems increasingly face multiple and interacting stressors, the incorporation of organismal thermal limits into conservation design emerges as a necessary foundation for equitable, effective and future-proof ocean stewardship.

4.4. Limitations and Perspectives

Our study relies on a single representative species (*M. galloprovincialis*). In reality, interspecific trait variations (such as shell color, body size, and aggregating behavior) can significantly alter local heat budgets. Consequently, our single-species baseline may locally over- or underestimate thermal risks. Future large-scale HBM studies should integrate morphological data from multiple species to improve local risk assessment.

Although the biophysical model has a strong global transferability, it may still neglect errors caused by local environmental input forcings (e.g., complex local wave run-up) due to model validation being conducted only along the west coast of the United States. To bridge this gap, there is an urgent need to establish a standardized intertidal body temperature monitoring network along global coastlines.

The application of uniform thermal risk thresholds, which overlooks local adaptation among global populations. Consequently, this absolute metric may underestimate realized physiological risks in polar regions and overestimate them in highly heat-adapted areas. Future large-scale models should integrate spatially explicit thermal tolerance limits for more accurate physiological risk predictions.

Due to the continuous hourly environmental data being strictly required to capture tidal-driven thermal extremes in highly dynamic intertidal zones, we constrained global models to coarser spatial resolutions. It leads to overlooking buffering or amplification effects in local topography. Future biophysical models will benefit from the development of novel remote sensing or reanalysis data sets with ultra-high spatiotemporal resolution. By integrating thermal stress across diverse microhabitats within a region, risk assessments can be conducted with greater precision.

5. Conclusions

Global-scale hindcast body temperatures are essential for quantifying the thermal risks faced by intertidal species. Our findings indicate that most coastal mussel populations are subject to diverse thermal risks. The spatial patterns of thermal risk metrics exhibit a patchy, mosaic-like distribution, while semi-enclosed seas and regions influenced by western boundary currents amplify thermal stress, substantially affecting the patch distribution of thermal risk along global coastlines. By integrating multiple thermal metrics, this study provides a comprehensive evaluation of intertidal thermal vulnerability, offering valuable insights into spatial variability and informing conservation strategies for intertidal ecosystems worldwide.

Conflict of Interest

The authors declare no conflicts of interest relevant to this study.

Availability Statement

Raw and processed data and all code needed to reproduce the analyses are available in (Ma et al., 2025). Climate data in NCEP Climate Forecast System Reanalysis (CFSR) and NCEP Climate Forecast System Version 2 (CFSv2) are provided by (Saha et al., 2010, 2011). The ECMWF (European Centre for Medium-Range Weather Forecasts) Reanalysis 5th Generation data set (ERA5) are available in (Hersbach et al., 2023). Robomussels data were obtained from (Helmuth et al., 2017). Species distribution data can be obtained from the Global Biodiversity Information Facility (GBIF.org, 2025) and the Ocean Biodiversity Information System (OBIS.org, 2025).

Acknowledgments

We thank George N. Somero of Hopkins Marine Station, Stanford University, for his insightful suggestions on thermal physiology and for his valuable contributions to improving the manuscript. We thank Xiao-Lu Zhu from Ocean University of China for her assistance with data acquisition and data visualization. This study is supported by the National Key Research and Development Program of China (2025YFE0102400), the National Natural Science Foundation of China (42025604), the Fundamental Research Program of Shandong Province (JCYJTQ-hYKX-2026-02), and the Fundamental Research Funds for the Central Universities.

References

Bagne, K. E., Friggens, M. M., & Finch, D. M. (2011). *A system for assessing vulnerability of species (SAVS) to climate change*. Gen. Technical Report RMRS-GTR-257 (Vol. 28, p. 257). US Department of Agriculture, Forest Service, Rocky Mountain Research Station. https://doi.org/10.2737/RMRS-GTR-257

Bilajac, A., Gljušćić, E., Smith, S., Najdek, M., & Iveša, L. (2024). Effects of extreme temperatures and recovery potential of Gongolaria barbata from a coastal lagoon in the northern Adriatic Sea: An ex situ approach. *Annals of Botany*, *134*(3), mcae038. https://doi.org/10.1093/aob/mcae038

Boyce, D. G., Tittensor, D. P., Garilao, C., Henson, S., Kaschner, K., Kesner-Reyes, K., et al. (2022). A climate risk index for marine life. *Nature Climate Change*, *12*(9), 854–862. https://doi.org/10.1038/s41558-022-01437-y

Cavaleri, L., Balsamo, G., Beljaars, A., Bertotti, L., Davison, S., Edwards, J., et al. (2024). ECMWF and UK Met Office offshore blowing winds: Impact of horizontal resolution and coastal orography. *Journal of Geophysical Research: Atmospheres*, *129*(6), e2023JD039673. https://doi.org/10.1029/2023JD039673

Coelho, J., Court, M., Otjacques, E., Lopes, V. M., Paula, J. R., Repolho, T., et al. (2023). Effects of tidal emersion and marine heatwaves on cuttlefish early ontogeny. *Marine Biology*, *170*(1), 3. https://doi.org/10.1007/s00227-022-04150-8

Colton, M. A., McManus, L. C., Schindler, D. E., Mumby, P. J., Palumbi, S. R., Webster, M. M., et al. (2022). Coral conservation in a warming world must harness evolutionary adaptation. *Nature Ecology & Evolution*, *6*(10), 1405–1407. https://doi.org/10.1038/s41559-022-01854-4

Denny, M. W., & Dowd, W. W. (2012). Biophysics, environmental stochasticity, and the evolution of thermal safety margins in intertidal limpets. *Journal of Experimental Biology*, *215*(6), 934–947. https://doi.org/10.1242/jeb.058958

Denny, M. W., & Harley, C. D. G. (2006). Hot limpets: Predicting body temperature in a conductance-mediated thermal system. *Journal of Experimental Biology*, *209*(13), 2409–2419. https://doi.org/10.1242/jeb.02257

Dong, Y., Li, X., Choi, F. M., Williams, G. A., Somero, G. N., & Helmuth, B. (2017). Untangling the roles of microclimate, behaviour and physiological polymorphism in governing vulnerability of intertidal snails to heat stress. *Proceedings of the Royal Society B: Biological Sciences*, *284*(1854), 20162367. https://doi.org/10.1098/rspb.2016.2367

Ek, M., Mitchell, K., Lin, Y., Rogers, E., Grunmann, P., Koren, V., et al. (2003). Implementation of Noah land surface model advances in the National Centers for Environmental Prediction operational mesoscale Eta model. *Journal of Geophysical Research*, *108*(D22). https://doi.org/10.1029/2002JD003296

Feng, X., Haines, K., & de Boisséson, E. (2018). Coupling of surface air and sea surface temperatures in the CERA-20C reanalysis. *Quarterly Journal of the Royal Meteorological Society*, *144*(710), 195–207. https://doi.org/10.1002/qj.3194

Fitzhenry, T., Halpin, P. M., & Helmuth, B. (2004). Testing the effects of wave exposure, site, and behavior on intertidal mussel body temperatures: Applications and limits of temperature logger design. *Marine Biology*, *145*(2), 339–349. https://doi.org/10.1007/s00227-004-1318-6

Foulk, A., Gouhier, T., Choi, F., Torossian, J. L., Matzelle, A., Sittenfeld, D., & Helmuth, B. (2024). Physiologically informed organismal climatologies reveal unexpected spatiotemporal trends in temperature. *Conservation Physiology*, *12*(1), coae025. https://doi.org/10.1093/conphys/coae025

Fraser, A. K. L. (2023). *Movement and microhabitat use of intertidal snails during active summer months*. Thompson Rivers University.

GBIF.org. (2025). GBIF occurrence download [Dataset]. *GBIF.org*. Retrieved from https://www.gbif.org/occurrence/download?taxon_key=2285679&year=1980,2023&occurrence_status=present

Gilman, S., Harley, C. D. G., Strickland, D., Vanderstraeten, O., O'Donnell, M., & Helmuth, B. (2006). Evaluation of effective shore level as a method of characterizing intertidal wave exposure regimes. *Limnology and Oceanography: Methods*, *4*(11), null-457. https://doi.org/10.4319/lom.2006.4.448

Greene, C. A., Erofeeva, S., Padman, L., Howard, S. L., Sutterley, T., & Egbert, G. (2024). Tide model driver for MATLAB. *Journal of Open Source Software*, *9*(95), 6018. https://doi.org/10.21105/joss.06018

23284277, 2026, 5, Downloaded from https://agupubs.onlinelibrary.wiley.com/doi/10.1029/2025EF007645 by University Degli Studi Di Pale, Wiley Online Library on [09/07/2026]. See the Terms and Conditions (https://onlinelibrary.wiley.com/terms-and-conditions) on Wiley Online Library for rules of use; OA articles are governed by the applicable Creative Commons License

Halpin, P. M., Menge, B. A., & Hofmann, G. E. (2004). Experimental demonstration of plasticity in the heat shock response of the intertidal mussel Mytilus californianus. *Marine Ecology Progress Series*, *276*, 137–145. https://doi.org/10.3354/meps276137

Harley, C. D. G. (2008). Tidal dynamics, topographic orientation, and temperature-mediated mass mortalities on rocky shores. *Marine Ecology Progress Series*, *371*, 37–46. https://doi.org/10.3354/meps07711

Hart-Davis, M. G., Piccioni, G., Dettmering, D., Schwatke, C., Passaro, M., & Seitz, F. (2021). EOT20: A global ocean tide model from multi-mission satellite altimetry. *Earth System Science Data*, *13*(8), 3869–3884. https://doi.org/10.5194/essd-13-3869-2021

Hawkins, S. J., Moore, P. J., Burrows, M. T., Poloczanska, E., Mieszkowska, N., Herbert, R. J. H., et al. (2008). Complex interactions in a rapidly changing world: Responses of rocky shore communities to recent climate change. *Climate Research*, *37*(2–3), 123–133. https://doi.org/10.3354/cr00768

Helmuth, B. (1998). Intertidal mussel microclimates: Predicting the body temperature of a sessile invertebrate. *Ecological Monographs*, *68*(1), 51–74. https://doi.org/10.1890/0012-9615(1998)068[0051:IMMPTB]2.0.CO;2

Helmuth, B. (1999). Thermal biology of rocky intertidal mussels: Quantifying body temperatures using climatological data. *Ecology*, *80*(1), 15–34. https://doi.org/10.1890/0012-9658(1999)080[0015:Tborim]2.0.Co;2

Helmuth, B., Broitman, B. R., Blanchette, C. A., Gilman, S., Halpin, P., Harley, C. D., et al. (2006). Mosaic patterns of thermal stress in the rocky intertidal zone: Implications for climate change. *Ecological Monographs*, *76*(4), 461–479. https://doi.org/10.1890/0012-9615(2006)076[0461:MPOTSI]2.0.CO;2

Helmuth, B., Choi, F., Matzelle, A., Torossian, J. L., Morello, S. L., Mislan, K. A., et al. (2016). Long-term, high frequency in situ measurements of intertidal mussel bed temperatures using biomimetic sensors. *Scientific Data*, *3*(1), 160087. https://doi.org/10.1038/sdata.2016.87

Helmuth, B., Choi, F., Matzelle, A., Torossian, J. L., Morello, S. L., Mislan, K. A., et al. (2017). Data from: Long-term, high frequency in situ measurements of intertidal mussel bed temperatures using biomimetic sensors [Dataset]. *Dryad*. https://doi.org/10.5061/dryad.6n8kf

Helmuth, B., Harley, C. D. G., Halpin, P. M., O'Donnell, M., Hofmann, G. E., & Blanchette, C. A. (2002). Climate change and latitudinal patterns of intertidal thermal stress. *Science*, *298*(5595), 1015–1017. https://doi.org/10.1126/science.1076814

Helmuth, B., Yamane, L., Lalwani, S., Matzelle, A., Tockstein, A., & Gao, N. (2011). Hidden signals of climate change in intertidal ecosystems: What (not) to expect when you are expecting. *Journal of Experimental Marine Biology and Ecology*, *400*(1), 191–199. https://doi.org/10.1016/j.jembe.2011.02.004

Hersbach, H., Bell, B., Berrisford, P., Biavati, G., Horányi, A., Muñoz Sabater, J., et al. (2023). ERA5 hourly data on single levels from 1940 to present [Dataset]. *Copernicus Climate Change Service (C3S) Climate Data Store (CDS)*. https://doi.org/10.24381/cds.adbb2d47

Holbrook, N. J., Scannell, H. A., Sen Gupta, A., Benthuysen, J. A., Feng, M., Oliver, E. C., et al. (2019). A global assessment of marine heatwaves and their drivers. *Nature Communications*, *10*(1), 2624. https://doi.org/10.1038/s41467-019-10206-z

Ioannidis, E., Lolis, C. J., Papadimas, C. D., Hatzianastassiou, N., & Bartzokas, A. (2018). On the intra-annual variation of cloudiness over the Mediterranean region. *Atmospheric Research*, *208*, 246–256. https://doi.org/10.1016/j.atmosres.2017.08.021

IPCC. (2021). Annex I: Observational products. In V. Masson-Delmotte, P. Zhai, A. Pirani, S. L. Connors, C. Péan, et al. (Eds.), *Climate change 2021: The physical science basis. Contribution of working group I to the sixth assessment report of the intergovernmental panel on climate change* (pp. 2061–2086). Cambridge University Press.

IUCN. (2024). The IUCN red list of threatened species. Retrieved from http://www.iucnredlist.org

Jurgens, L., & Gaylord, B. (2018). Physical effects of habitat-forming species override latitudinal trends in temperature. *Ecology Letters*, *21*(2), 190–196. https://doi.org/10.1111/ele.12881

Kroeker, K. J., Sanford, E., Rose, J. M., Blanchette, C. A., Chan, F., Chavez, F. P., et al. (2016). Interacting environmental mosaics drive geographic variation in mussel performance and predation vulnerability. *Ecology Letters*, *19*(7), 771–779. https://doi.org/10.1111/ele.12613

Larson, J. G., Thompson, D. W., & Hurrell, J. W. (2024). Signature of the western boundary currents in local climate variability. *Nature*, *634*(8035), 862–867. https://doi.org/10.1038/s41586-024-08019-2

Lefcheck, J. S. (2016). piecewiseSEM: Piecewise structural equation modelling in r for ecology, evolution, and systematics. *Methods in Ecology and Evolution*, *7*(5), 573–579. https://doi.org/10.1111/2041-210X.12512

Li, X.-x., Tan, Y., Sun, Y.-x., Wang, J., & Dong, Y.-w. (2021). Microhabitat temperature variation combines with physiological variation to enhance thermal resilience of the intertidal mussel Mytilisepta virgata. *Functional Ecology*, *35*(11), 2497–2507. https://doi.org/10.1111/1365-2435.13885

Lima, F. P., & Wethey, D. S. (2009). Robolimpets: Measuring intertidal body temperatures using biomimetic loggers. *Limnology and Oceanography: Methods*, *7*(5), 347–353. https://doi.org/10.4319/lom.2009.7.347

Ma, L. X., Foulk, A., Sarà, G., Chen, X.-Y., Helmuth, B., & Dong, Y.-W. (2025). Data and code from: Hindcast body temperature reveals sites of amplified thermal risk in global Coastlines [Dataset]. *Dryad*. https://doi.org/10.5061/dryad.r7sqv9sph

Ma, L. X., Wang, J., Denny, M. W., & Dong, Y. W. (2024). Hindcasted body temperatures reveal underestimated thermal stress faced by intertidal species. *Global Ecology and Biogeography*, *33*(11), e13908. https://doi.org/10.1111/geb.13908

Miller, L. P., & Denny, M. W. (2011). Importance of behavior and morphological traits for controlling body temperature in littorinid snails. *The Biological Bulletin*, *220*(3), 209–223. https://doi.org/10.1086/BBLv220n3p209

Mislan, K. A. S., Wethey, D. S., & Helmuth, B. (2009). When to worry about the weather: Role of tidal cycle in determining patterns of risk in intertidal ecosystems. *Global Change Biology*, *15*(12), 3056–3065. https://doi.org/10.1111/j.1365-2486.2009.01936.x

OBIS.org. (2025). OBIS occurrence download [Dataset]. *OBIS.org*. Retrieved from https://obis.org/taxon/138228

Pigot, A. L., Merow, C., Wilson, A., & Trisos, C. H. (2023). Abrupt expansion of climate change risks for species globally. *Nature Ecology & Evolution*, *7*(7), 1060–1071. https://doi.org/10.1038/s41559-023-02070-4

Pinheiro, J., Bates, D., DebRoy, S., Sarkar, D., Heisterkamp, S., Van Willigen, B., & Maintainer, R. (2011). nlme: Linear and nonlinear mixed effects models. *R package version*.

Pottier, P., Kearney, M. R., Wu, N. C., Gunderson, A. R., Rej, J. E., Rivera-Villanueva, A. N., et al. (2025). Vulnerability of amphibians to global warming. *Nature*, *639*(8056), 1–8. https://doi.org/10.1038/s41586-025-08665-0

Queirós, A. M., Talbot, E., Beaumont, N. J., Somerfield, P. J., Kay, S., Pascoe, C., et al. (2021). Bright spots as climate-smart marine spatial planning tools for conservation and blue growth. *Global Change Biology*, *27*(21), 5514–5531. https://doi.org/10.1111/geb.15827

Raymond, W. W., Barber, J. S., Dethier, M. N., Hayford, H. A., Harley, C. D. G., King, T. L., et al. (2022). Assessment of the impacts of an unprecedented heatwave on intertidal shellfish of the Salish Sea. *Ecology*, *103*(10), e3798. https://doi.org/10.1002/ecy.3798

Saha, S., Moorthi, S., Pan, H.-L., Wu, X., Wang, J., Nadiga, S., et al. (2010). NCEP Climate Forecast System Reanalysis (CFSR) selected hourly time-series products, January 1979 to December 2010 [Dataset]. *Research Data Archive at the National Center for Atmospheric Research, Computational and Information Systems Laboratory*. https://doi.org/10.5065/D6513W89

23284277, 2026, 5, Downloaded from https://agupubs.onlinelibrary.wiley.com/doi/10.1029/2025EF007645 by University Degli Studi Di Pale, Wiley Online Library on [09/07/2026]. See the Terms and Conditions (https://onlinelibrary.wiley.com/terms-and-conditions) on Wiley Online Library for rules of use; OA articles are governed by the applicable Creative Commons License

Saha, S., Moorthi, S., Wu, X., Wang, J., Nadiga, S., Tripp, P., et al. (2011). NCEP climate forecast system version 2 (CFSv2) selected hourly time-series products [Dataset]. *Research Data Archive at the National Center for Atmospheric Research, Computational and Information Systems Laboratory*. https://doi.org/10.5065/D6N877VB

Sampaio, L., Moreira, J., Rubal, M., Guerrero-Meseguer, L., & Veiga, P. (2022). A review of coastal anthropogenic impacts on mytilid mussel beds: Effects on mussels and their associated assemblages. *Diversity*, *14*(5), 409. https://doi.org/10.3390/d14050409

Sánchez-Velasco, L., Gutiérrez-Moreno, D. C., Jiménez-Rosenberg, S. P. A., Camacho-Gastélum, R., & Godínez, V. M. (2025). Fish larvae distribution and hydrographic processes off Cabo Pulmo National Park, entrance of the Gulf of California, during an oceanographic cruise (October 2022). *Regional Studies in Marine Science*, 104430. https://doi.org/10.1016/j.rsma.2025.104430

Seabra, R. (2024). CCTBON - Coupled coastal temperature and biodiversity observation network [Dataset]. *Zenodo*. https://doi.org/10.5281/zenodo.13850514

Seabra, R., Varela, R., Santos, A. M., Gómez-Gesteira, M., Meneghesso, C., Wethey, D. S., & Lima, F. P. (2019). Reduced nearshore warming associated with eastern boundary upwelling systems. *Frontiers in Marine Science*, *6*, 104. https://doi.org/10.3389/fmars.2019.00104

Seabra, R., Wethey, D., Santos, A. M., & Lima, F. (2011). Side matters: Microhabitat influence on intertidal heat stress over a large geographical scale. *Journal of Experimental Marine Biology and Ecology*, *400*, 200–208.

Seuront, L., Nicastro, K. R., Zardi, G. I., & Goberville, E. (2019). Decreased thermal tolerance under recurrent heat stress conditions explains summer mass mortality of the blue mussel Mytilus edulis. *Scientific Reports*, *9*(1), 17498. https://doi.org/10.1038/s41598-019-53580-w

Shumway, R. H., Stoffer, D. S., Shumway, R. H., Stoffer, D. S., & Springer International Publishing. (2017). ARIMA models. In *Time series analysis its applications: With R examples* (pp. 75–163).

Shunk, N. P., Mazzini, P. L., & Walter, R. K. (2024). Impacts of marine heatwaves on subsurface temperatures and dissolved oxygen in the Chesapeake Bay. *Journal of Geophysical Research: Oceans*, *129*(3), e2023JC020338. https://doi.org/10.1029/2023JC020338

Sinclair, B. J., Marshall, K. E., Sewell, M. A., Levesque, D. L., Willett, C. S., Slotsbo, S., et al. (2016). Can we predict ectotherm responses to climate change using thermal performance curves and body temperatures? *Ecology Letters*, *19*(11), 1372–1385. https://doi.org/10.1111/ele.12686

Spalding, M. D., Fox, H. E., Allen, G. R., Davidson, N., Ferdaña, Z. A., Finlayson, M., et al. (2007). Marine ecoregions of the world: A bioregionalization of coastal and shelf areas. *BioScience*, *57*(7), 573–583. https://doi.org/10.1641/B570707

Stock, C. A., Pegion, K., Vecchi, G. A., Alexander, M. A., Tommasi, D., Bond, N. A., et al. (2015). Seasonal sea surface temperature anomaly prediction for coastal ecosystems. *Progress in Oceanography*, *137*, 219–236. https://doi.org/10.1016/j.pocean.2015.06.007

Sully, S., Hodgson, G., & van Woesik, R. (2022). Present and future bright and dark spots for coral reefs through climate change. *Global Change Biology*, *28*(15), 4509–4522. https://doi.org/10.1111/gcb.16083

Szathmary, P., Helmuth, B., & Wethey, D. (2009). Climate change in the rocky intertidal zone: Predicting and measuring the body temperature of a keystone predator. *Marine Ecology Progress Series*, *374*, 43–56. https://doi.org/10.3354/meps07682

Tagliarolo, M., & McQuaid, C. D. (2015). Sub-lethal and sub-specific temperature effects are better predictors of mussel distribution than thermal tolerance. *Marine Ecology Progress Series*, *535*, 145–159. https://doi.org/10.3354/meps11434

Talley, L. D. (2011). *Descriptive physical oceanography: An introduction*. Academic Press.

Trew, B. T., & Maclean, I. M. (2021). Vulnerability of global biodiversity hotspots to climate change. *Global Ecology and Biogeography*, *30*(4), 768–783. https://doi.org/10.1111/geb.13272

Wethey, D. S., Brin, L. D., Helmuth, B., & Mislan, K. A. S. (2011). Predicting intertidal organism temperatures with modified land surface models. *Ecological Modelling*, *222*(19), 3568–3576. https://doi.org/10.1016/j.ecolmodel.2011.08.019

White, R. H., Anderson, S., Booth, J. F., Braich, G., Draeger, C., Fei, C., et al. (2023). The unprecedented Pacific northwest heatwave of June 2021. *Nature Communications*, *14*(1), 727. https://doi.org/10.21203/rs.3.rs-1520351/v1

Wilson, L. J., Fulton, C. J., Hogg, A. M., Joyce, K. E., Radford, B. T. M., & Fraser, C. I. (2016). Climate-driven changes to ocean circulation and their inferred impacts on marine dispersal patterns. *Global Ecology and Biogeography*, *25*(8), 923–939. https://doi.org/10.1111/geb.12456

Wu, L., Cai, W., Zhang, L., Nakamura, H., Timmermann, A., Joyce, T., et al. (2012). Enhanced warming over the global subtropical western boundary currents. *Nature Climate Change*, *2*(3), 161–166. https://doi.org/10.1038/nclimate1353

Yang, H., Guo, H., Chen, Z., Cai, W., Wu, L., Cai, J., et al. (2025). Onshore intensification of subtropical western boundary currents in a warming climate. *Nature Climate Change*, *15*(3), 1–7. https://doi.org/10.1038/s41558-025-02258-5

Young, I. R., Kirezci, E., & Ribal, A. (2020). The global wind resource observed by scatterometer. *Remote Sensing*, *12*(18), 2920. https://doi.org/10.3390/rs12182920

Zhang, H., Shen, Y., & Tang, J. (2021). Hydrodynamics and water renewal in the Pearl River Estuary, China: A numerical study from the perspective of water age. *Ocean Engineering*, *237*, 109639. https://doi.org/10.1016/j.oceaneng.2021.109639

Zhang, T., Tian, B., Wang, Y., Liu, D., Sun, S., Duan, Y., & Zhou, Y. (2021). Quantifying seasonal variations in microphytobenthos biomass on estuarine tidal flats using Sentinel-1/2 data. *Science of the Total Environment*, *777*, 146051. https://doi.org/10.1016/j.scitotenv.2021.146051

eeblab www.unipa.it/gsaralab courtesy copy not for commercial use

23284277, 2026, 5, Downloaded from https://agupubs.onlinelibrary.wiley.com/doi/10.1029/2025EF007645 by University Degli Studi Di Pale, Wiley Online Library on [09/07/2026]. See the Terms and Conditions (https://onlinelibrary.wiley.com/terms-and-conditions) on Wiley Online Library for rules of use; OA articles are governed by the applicable Creative Commons License